*Journal of Advanced Ceramics*
2023, **12**(4): 747–759
https://doi.org/10.26599/JAC.2023.9220717
ISSN 2226-4108
CN 10-1154/TQ

**Research Article**

# Oxygen vacancy-rich $MoO_3$ nanorods as photocatalysts for photo-assisted Li–$O_2$ batteries

Guiru Sun, Daming Yang, Zexu Zhang, Yan Wang, Wei Lu, Ming Feng*

*Key Laboratory of Functional Materials Physics and Chemistry of the Ministry of Education, Jilin Normal University, Changchun 130103, China*

Received: October 26, 2022; Revised: December 16, 2022; Accepted: January 4, 2023


**Abstract:** Photo-assisted lithium–oxygen (Li–$O_2$) batteries have been developed as a new system to reduce a large overpotential in the Li–$O_2$ batteries. However, constructing an optimized photocatalyst is still a challenge to achieve broad light absorption and a low recombined rate of photoexcited electrons and holes. Herein, oxygen vacancy-rich molybdenum trioxide ($MoO_{3-x}$) nanorods are employed as photocatalysts to accelerate kinetics of cathode reactions in the photo-assisted Li–$O_2$ batteries. Oxygen vacancies on the $MoO_{3-x}$ nanorods can not only increase light-harvesting capability but also improve electrochemical activity for the cathode reactions. Under illumination, the photoexcited electrons and holes are effectively separated on the $MoO_{3-x}$ nanorods. During discharging, activated $O_2$ is reduced to $Li_2O_2$ by the photoexcited electrons from the $MoO_{3-x}$ nanorods. The photoexcited holes can promote the decomposition of $Li_2O_2$ during subsequent charging. Accordingly, the photo-assisted Li–$O_2$ batteries with the $MoO_{3-x}$ nanorods deliver an ultralow overpotential of 0.22 V, considerable rate capability, and good reversibility. We think that this work could give a reference for the exploitation and application of the photocatalysts in the photo-assisted Li–$O_2$ batteries.

**Keywords:** molybdenum trioxide ($MoO_3$) nanorods; oxygen vacancy; photocatalyst; photo-assistance; lithium–oxygen (Li–$O_2$) batteries

## 1 Introduction

Lithium–oxygen (Li–$O_2$) batteries are a promising energy storage system due to its high theoretical energy density (~3500 Wh·kg$^{-1}$), which are operated with $Li_2O_2$-redox reaction ($2Li^+ + O_2 + 2e^- \leftrightarrow Li_2O_2$, $E^0$ = 2.96 V, where $E^0$ is the standard electrode potential of the Li–$O_2$ batteries) [1–3]. Unfortunately, the Li–$O_2$ batteries face many tough problems, among which sluggish kinetics of a cathode lead to large overpotential, low round-trip efficiency, and limited cycle of the Li–$O_2$ batteries [4–6]. It is reported that the sluggish kinetics are associated with a passivated cathode surface by $Li_2O_2$. The generated $Li_2O_2$ will obstruct a charge transfer and hinder $O_2$ diffusion on the cathode because it is a wide-band gap insulator and does not dissolve in an electrolyte [7–9]. To improve the reaction kinetics, some electrocatalysts (e.g., noble metal- and transition metal-based materials) were introduced in the cathode [9–12]. Unfortunately, rare and expensive noble metals and the limited catalytic activity of transition metals hinder their widely practical applications. Thus, it is expected to seek cut-price and flexible means for accelerating the reaction kinetics of the Li–$O_2$ batteries.

* Corresponding author.
E-mail: mingfeng@jlnu.edu.cn

Recently, the employment of light has been proven that can promote the generation and oxidation of $Li_2O_2$, especially reduce the overpotential in the photo-assisted Li–$O_2$ batteries [13–16]. Under light irradiation, a semiconductor-containing cathode contributes to separating the electrons and holes in conduction bands (CBs) and valence bands (VBs), respectively [15–18]. In an ideal system, the photoelectrons are able to boost the formation of $Li_2O_2$ during oxygen reduction reaction (ORR), while the holes could facilitate the decomposition of $Li_2O_2$ during oxygen evolution reaction (OER) [19]. Thus, the semiconductor catalyst is regarded as the key that affects the performance of the photo-assisted Li–$O_2$ batteries [20]. Among the family of semiconductor materials, orthorhombic molybdenum trioxide (α-$MoO_3$) as the photocatalyst plays a major role in the field of photocatalysis because of its nontoxicity, low price, and good chemical stability [21,22]. Various morphologies and structures of $MoO_3$ were developed to improve their photocatalytic activity, such as nanobelts [23], nanorods [24], and nanotubes [25]. Unfortunately, these $MoO_3$ species show low photocatalytic ability in practical applications under visible light, which could result from two reasons: (i) $MoO_3$ as an n-type semiconductor with a wide band gap ($E_g$ = 3.2 eV) has a low utilization rate for visible light [26]; (ii) the photoexcited electrons and holes easily recombine [27]. Therefore, it is highly desirable to broaden the range of light absorption and improve separation efficiency of the electrons and holes for enhancing the photocatalytic activity of $MoO_3$.

To address the mentioned challenges, the research focused on the construction of defect engineering (usually oxygen defects) to improve the photocatalytic performance of the semiconductor materials by tuning their electronic structures and surface properties [28]. Very recently, we demonstrated that titanium dioxide ($TiO_2$) as the photocatalyst shows superior catalytic ability in the photo-assistance Li–$O_2$ batteries by introducing oxygen vacancies [14]. It is expected to obtain a similar effect for $MoO_3$ with the oxygen vacancies (i.e., $MoO_{3-x}$). More importantly, it has been proved that the oxygen vacancies in $MoO_3$ interact strongly with active oxygen from the battery environment (e.g., $O_2$, $LiO_2$, and $Li_2O_2$), which plays a key role during the discharge and charge processes of Li–$O_2$ batteries [29]. Although the photocatalytic behavior of $MoO_{3-x}$ has been reported by previous works [26,27], its catalytic mechanism in the photo-assisted Li–$O_2$ batteries has rarely been mentioned. Therefore, it is significant for the employment of $MoO_{3-x}$ as the photocatalyst and for understanding its catalytic mechanism in the photo-assisted Li–$O_2$ batteries.

In this study, the $MoO_{3-x}$ nanorods were fabricated by combining solvothermal and hydrogen-thermal reduction methods, which were used as the photocatalysts in the photo-assisted Li–$O_2$ batteries. By introducing the oxygen vacancies, the light response and photocatalytic ability of the $MoO_{3-x}$ nanorods are significantly increased. The photoexcited electrons and holes on the $MoO_{3-x}$ nanorods were separated effectively with light irradiation. The photoexcited electrons are beneficial to the $O_2$ reduction to form $Li_2O_2$ during discharge. The generated $Li_2O_2$ is decomposed to $O_2$ and $Li^+$ ions by the holes during charging. The photo-assisted Li–$O_2$ batteries with the $MoO_{3-x}$ nanorods showed an ultralow overpotential of 0.22 V, good rate performance, and superior reversibility. This work could offer an opportunity for the design of highly active photocatalysts in the photo-assisted Li–$O_2$ batteries.

## 2 Experimental

### 2.1 Chemicals and materials

All reagents and solvents, such as hydrogen peroxide ($H_2O_2$; analytical reagent (AR) (30%), Sinopharm Chemical Reagent Co., Ltd.), nitric acid ($HNO_3$; AR, Sinopharm Chemical Reagent Co., Ltd.), $MoO_3$ (AR, Aladdin Reagent), and Li foil (China Energy Lithium Co., Ltd.), were commercially available. Tetraethylene glycol dimethyl ether (TEGDME; AR (99.7%), Aladdin Reagent) and N-methyl-pyrrolidone (NMP; AR (99%), Aladdin Reagent) were dried with activated molecular sieves (Type 4 Å, Sinopharm Chemical Reagent Co., Ltd.) for 7 d. Carbon paper (CP; CeTech Co., Ltd.), super P (SP; ~50 nm, Timcal), polyvinylidene fluoride (PVDF; 99.9%, DuPont Company), lithium bis (trifluoromethane sulfonimide) (LiTFSI; AR, Aladdin Reagent), and glass fiber (GF) separator (GF/D, Whatman) were dried under a vacuum oven (120 ℃, 24 h).

### 2.2 Preparation of $MoO_{3-x}$ nanorods

$MoO_3$ (3.6 g) was added into $H_2O_2$ (27 mL) to form solution by vigorous stirring. $HNO_3$ (13.5 mL) and distilled water (65 mL) were then mixed with the above solution. After stirring for 30 min, the obtained mixture was transferred to a Teflon-lined autoclave (50 mL) and heated at 170 ℃ for 24 h. The precipitate

was separated by centrifugation, washing, and drying (50 ℃ for 24 h), which is the $MoO_3$ nanorods. The $MoO_{3-x}$ nanorods were synthesized by reducing the $MoO_3$ nanorods in hydrogen-thermal environment at 350 ℃ for 2 h with $H_2$ and Ar mixture gas flow (8 : 92).

### 2. 3 Characterizations

An X-ray diffractometer (D/MAX-2500/PC, Rigaku) was employed to gather X-ray diffraction (XRD) patterns of all samples. Raman spectra of the products were acquired using a Micro Raman system (LabRAM HR spectrometer, Horiba) with an Ar ion laser (514 nm) and a microscope (BX, Olympus). An X-ray photoelectron spectrometer (ESCALAB 250Xi, Thermo Fisher Scientific) was used to examine valence states of elements. Microstructures and morphologies of all samples were identified by a scanning electron microscope (SEM; S-5500, Hitachi) and a transmission electron microscope (TEM; Talos F200X G2, Thermo Fisher Scientific) with an energy dispersive X-ray spectrometer and a high-angle annular dark field-scanning TEM (HAADF-STEM). Photoluminescence (PL) spectra of the as-prepared samples were recorded on a spectrofluorometer (F-4600, Hitachi) at 25 ℃ in ambient air. An ultraviolet–visible (UV–Vis) spectrophotometer (UV-3600, Shimadzu) was performed to collect UV–Vis absorption spectra of the as-prepared products. An electron spin resonance (ESR) spectrometer (JES-FA200, JELO) was utilized to monitor unpaired electrons in the as-prepared samples.

### 2. 4 Assembly of Li–$O_2$ cells

To obtain slurry, the SP, $MoO_{3-x}$ nanorods, and PVDF were added to the NMP at a weight ratio of 6 : 3 : 1. The cathodes were prepared by coating the slurry on the CP with a diameter of 13 mm and a thickness of ~20 μm, which were then dried in vacuum at 70 ℃ for 12 h for removing the excess solvent. Mass loadings of the SP and $MoO_{3-x}$ nanorods in the cathode are 0.2 and 0.1 mg, respectively. The 2025 coin-type cells were assembled using a Li foil anode (China Energy Lithium Co., Ltd.), a GF separator soaked in an electrolyte (135 μL, 1 M LiTFSI/TEGDME), and a cathode within an argon-filled glovebox (SG2400/750TS, Vigor, $H_2O$ and $O_2$ < 1 ppm). For the transmission of light and $O_2$, the cathode shells were punched to form a hole with a diameter of 10 mm.

### 2. 5 Electrochemical measurements

The obtained cells were tested in an $O_2$-filled glovebox (SG2400/750TS, Vigor, $H_2O$ and $O_2$ < 1 ppm) at various current density of 100–500 $mA \cdot g^{-1}$ under various fixed capacity of 500–1000 $mAh \cdot g^{-1}$ on system (CT-ZWJ-4'S-010, NEWARE). Note that the current density and specific capacity were calculated based on the mass of the SP. For testing photo-assisted Li–$O_2$ cells, a Xe lamp (gel-S500/350, Ceaulight) was employed as light source. The light intensity for the cathode surface was locked by fixing the power at 500 W. A testing platform of the photo-assisted Li–$O_2$ cells is shown in Fig. S1 in the Electronic Supplementary Material (ESM). Cyclic voltammetry (CV) curves were recorded at a scan rate of 0.1 $mV \cdot s^{-1}$ within a voltage ranging of 2.2–4.5 V vs. $Li/Li^+$. Linear sweep voltammetry (LSV) curves were obtained at a scan rate of 0.5 $mV \cdot s^{-1}$. Electrochemical impedance spectroscopy (EIS) was gathered within a frequency range of $10^{-2}$–$10^5$ Hz and an amplitude of 0.005 V. The CV curves, LSV curves, and EIS were performed on an electrochemical workstation (Solartron 1470E, AMETEK) at room temperature. A customized Swagelok type of the Li–$O_2$ cell with a quartz window and two polyetheretherketone (PEEK) capillary tubes was designed for differential electrochemical mass spectrometry (DEMS) on a commercial quadrupole mass spectrometer (HPR-20, Hiden).

## 3 Results and discussion

Crystal structures of $MoO_3$ and $MoO_{3-x}$ nanorods were evaluated, as shown in Fig. 1(a). XRD peaks could be assigned to the standard pattern of α-$MoO_3$ (JCPDS No. 05-0508) [26]. The main XRD peaks are consistent with the crystal planes of (020), (040), and (060), demonstrating highly preferred orientations. Compared with that of the pristine $MoO_3$ nanorods, the peak corresponding to the (040) crystal plane for the $MoO_{3-x}$ nanorods shifts to a higher angle (Fig. 1(b)), which arises from the expansion of an interlamellar spacing owing to the presence of the oxygen vacancies [27]. In Fig. 1(c), a set of typical Raman peaks are observed for $MoO_3$ and $MoO_{3-x}$ nanorods, which are consistent with Ref. [28]. The peaks at 280, 373, and 990 $cm^{-1}$ are ascribed to wagging vibration, bending vibration, and stretching vibration of terminal oxygen (Mo=O), respectively [30,31]. The peaks at 334 and 660 $cm^{-1}$ represent the bending vibration and stretching vibration of triple coordinated oxygen ($Mo_3$–O), respectively [32], and that at 818 $cm^{-1}$ could be caused by the stretching vibration of double coordinated

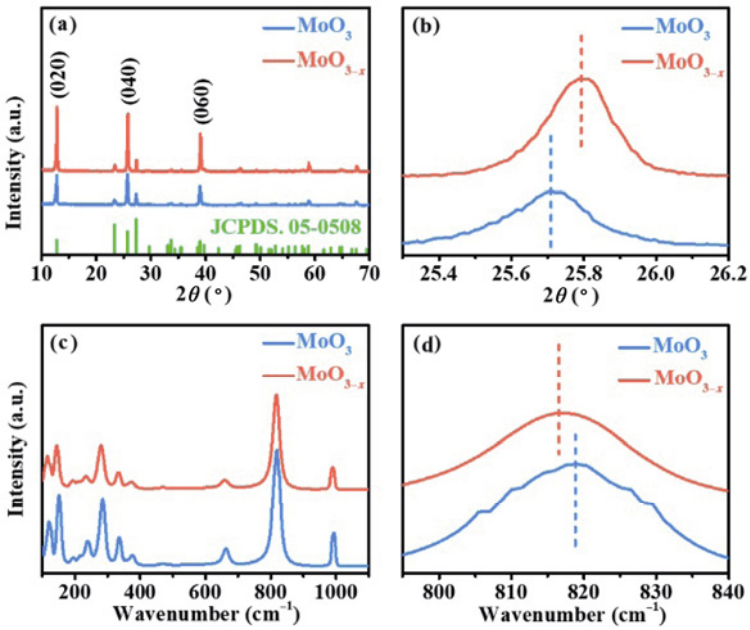


**Fig. 1** (a) XRD patterns and (b) corresponding magnified patterns of $MoO_3$ and $MoO_{3-x}$ nanorods; (c) Raman spectra and (d) corresponding magnified patterns of $MoO_3$ and $MoO_{3-x}$ nanorods.

oxygen ($Mo_2$–O) [33]. Note that a slight blue shift of the peak at 818 $cm^{-1}$ for the $MoO_{3-x}$ nanorods compared to that of the pristine $MoO_3$ nanorods was observed (Fig. 1(d)), resulting from phonon confinement by point defects [27,28].

Element compositions and states of $MoO_3$ and $MoO_{3-x}$ nanorods were evaluated by X-ray photoelectron spectroscopy (XPS). Survey spectra for both samples are displayed in Fig. 2(a), which shows the presence of Mo and O without any other elements. The atomic ratios are 1 : 3.33 and 1 : 2.84 for Mo and O in $MoO_3$ and $MoO_{3-x}$, respectively, confirming that the oxygen vacancies are successfully generated in the $MoO_{3-x}$ nanorods. In Fig. 2(b), the Mo 3d spectrum is deconvoluted into one pair of peaks at 232.9 and 236.0 eV for the $MoO_3$ nanorods, corresponding to Mo $3d_{5/2}$ and Mo $3d_{3/2}$ of $Mo^{6+}$, respectively [34]. In contrast, the Mo 3d spectra for the $MoO_{3-x}$ nanorods exhibit a new pair of peaks at 231.5 and 234.6 eV (Fig. 2(c)) that represent Mo $3d_{5/2}$ and Mo $3d_{3/2}$ of $Mo^{5+}$, respectively [35], implying the existence of the oxygen vacancies in the $MoO_{3-x}$ nanorods. The O 1s spectra for $MoO_3$ and $MoO_{3-x}$ nanorods are shown in Figs. 2(d) and 2(e), respectively, which can be deconvoluted into two peaks. The peak $O_1$ at 530.7 eV results from lattice oxygen. The peak $O_2$ at 532.3 eV is ascribed to surface chemisorbed oxygen. The area ratio of the peak $O_2$ to the peak $O_1$ for the $MoO_3$ nanorods is 0.59, which is lower than that for the $MoO_{3-x}$ nanorods (0.80), indicating that the oxygen vacancies contribute to increasing the surface adsorption of the oxygen species [36].

Morphologies and microstructures of $MoO_{3-x}$ were identified by the SEM and TEM. In Fig. 3(a), $MoO_3$ presents a uniform and rod-like nanostructure with a smooth surface. As shown in Fig. 3(b), the morphology of $MoO_{3-x}$ is the same as that of $MoO_3$, which indicates that the introduction of the oxygen vacancies does not affect the morphology. The length and width of $MoO_{3-x}$ nanorods were confirmed by the TEM images (Figs. 3(c) and 3(d), respectively). It can be seen that the length is ~9 μm (Fig. 3(c)), and the width is ~200 nm (Fig. 3(d)). In Fig. 3(e), the well-defined lattice fringes are observed for the $MoO_{3-x}$ nanorods. The interplanar distances are 2.332 and 2.702 Å, which are attributed to the (131) and (101) crystal planes of α-$MoO_3$ (JCPDS No. 05-0508), respectively [26]. Additionally, there are some disorder and discontinuous lattice fringes, as seen in the ellipse marks (Fig. 3(e)), which further proves the introduction of the oxygen vacancies in the $MoO_{3-x}$ nanorods. In Fig. 3(f), single-crystal nature is observed for the $MoO_{3-x}$ nanorods by a selected area electron diffraction (SAED) pattern. Equally, the exposed crystal planes of (200), (202), and (002) could be well indexed to α-$MoO_3$, which coincide well with the XRD results [26,28]. The unique morphology and element compositions of the $MoO_{3-x}$ nanorods are further revealed by the HAADF-STEM image (Fig. 3(g)) and

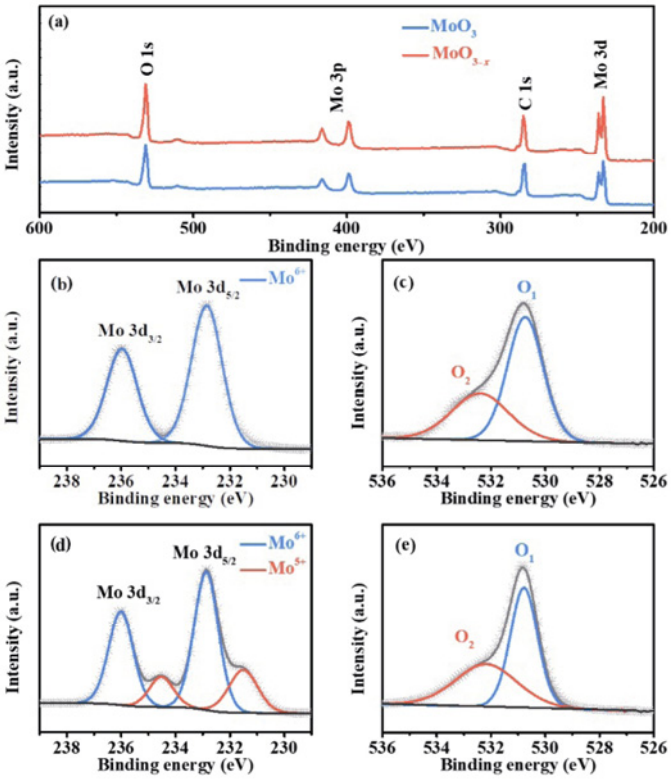


**Fig. 2** (a) XPS survey spectra of $MoO_3$ and $MoO_{3-x}$ nanorods; XPS spectra of (b, c) Mo 3d and (d, e) O 1s for $MoO_3$ nanorods and $MoO_{3-x}$ nanorods, respectively.

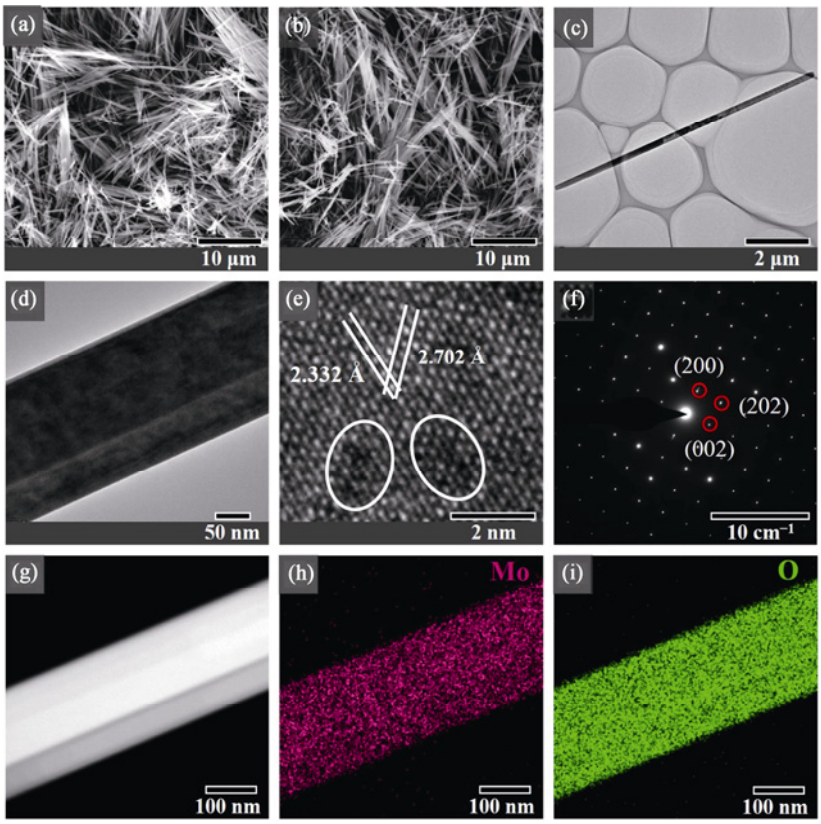


**Fig. 3** SEM images of (a) $MoO_3$ nanorods and (b) $MoO_{3-x}$ nanorods. (c, d) TEM images, (e) HRTEM image, (f) SAED pattern, (g) HAADF-STEM image, and (h, i) corresponding EDS elemental mapping images of $MoO_{3-x}$ nanorods.

energy-dispersive X-ray spectroscopy (EDS) elemental mappings (Figs. 3(h) and 3(i)). It clearly demonstrates that these elements of Mo and O are uniformly distributed on the $MoO_{3-x}$ nanorods. Note that the atomic ratio of Mo and O (1 : 2.97) is different from that of the XPS results (1 : 2.84). This could result from that the XPS is only surface sensitive.

To further verify the presence of the oxygen vacancies in the $MoO_{3-x}$ nanorods, the ESR spectra of the as-prepared $MoO_3$ and $MoO_{3-x}$ nanorods were recorded, as shown in Fig. 4(a). It can be seen that there is no visible ESR signal for the pristine $MoO_3$ nanorods. In sharp contrast, an intense signal of the spectral splitting factor $g$ at 2.003 is observed for the $MoO_{3-x}$ nanorods. The results suggest that the oxygen vacancies are successfully introduced into the $MoO_{3-x}$ nanorods [27,28]. The UV–Vis diffuse reflectance spectra of the as-prepared $MoO_3$ and $MoO_{3-x}$ nanorods were collected to evaluate optical absorption capacity of the photocatalyst. In Fig. 4(b), an absorption edge of the pristine $MoO_3$ nanorods is about 400 nm. Besides, no significant absorption is observed in the visible region. In contrast, the $MoO_{3-x}$ nanorods display strong absorption in the visible region, which results from the existence of the oxygen vacancies [27]. The $E_g$ of the $MoO_{3-x}$ nanorods is 3.24 eV, which is lower than that of the pristine $MoO_3$ nanorods (3.29 eV) (Fig. 4(c)), indicating that the oxygen vacancies could improve the photocatalytic activity [37]. The recombination feature of the photogenerated carriers in $MoO_3$ and $MoO_{3-x}$ nanorods was studied by the PL spectra. As shown in Fig. 4(d), there is a clear emission band at ~688 nm for both samples [38,39]. Note that the peak of the $MoO_3$ nanorods exhibits higher intensity than that of the $MoO_{3-x}$ nanorods, revealing that a recombination rate of the photoexcited electrons and holes is cut down after the introduction of the oxygen vacancies. Mott–Schottky plot of the $MoO_{3-x}$ nanorods displays a positive slope (Fig. 4(e)), suggesting that the $MoO_{3-x}$ nanorods are an n-type semiconductor [40]. The flat band potential ($V_{fb}$) of the $MoO_{3-x}$ nanorods is determined to be 2.75 V (vs. $Li^+/Li$), close to the CB for the n-type semiconductor [41]. According to the equation of $E_{VB} = E_{CB} + E_g$, the potentials of CB ($E_{CB}$) and VB ($E_{VB}$) for the $MoO_{3-x}$ nanorods are calculated to be 2.75 and 5.99 V (vs. $Li^+/Li$), respectively, which span an equilibrium potential of battery reaction (2.96 V vs. $Li^+/Li$) [42]. Additionally, the $E_{CB}$ and $E_{VB}$ of the $MoO_{3-x}$ nanorods can be calculated by the empirical equation [43]: $E_{VB} = X - E_e + 0.5E_g$, where $X$ (= 6.40 eV) is the absolute electronegativity of the $MoO_{3-x}$ nanorods [44], and $E_e$ (= 4.5 eV) is the energy of free electrons of the hydrogen scale [45]. According to the above equation, the $E_{VB}$ and $E_{CB}$ are calculated to be 6.00 and 2.76 V respectively, which are in accordance with the results calculated by the Mott–Schottky plot. Thereby, the $MoO_{3-x}$ nanorods will contribute to accelerating the ORR and OER processes under illumination, which is illustrated in Fig. 4(f). During discharge, the photoelectrons excited in the CB will boost the formation of $Li_2O_2$. Meantime, the holes are left in the VB and reduced via the electrons in an external circuit. During charging,

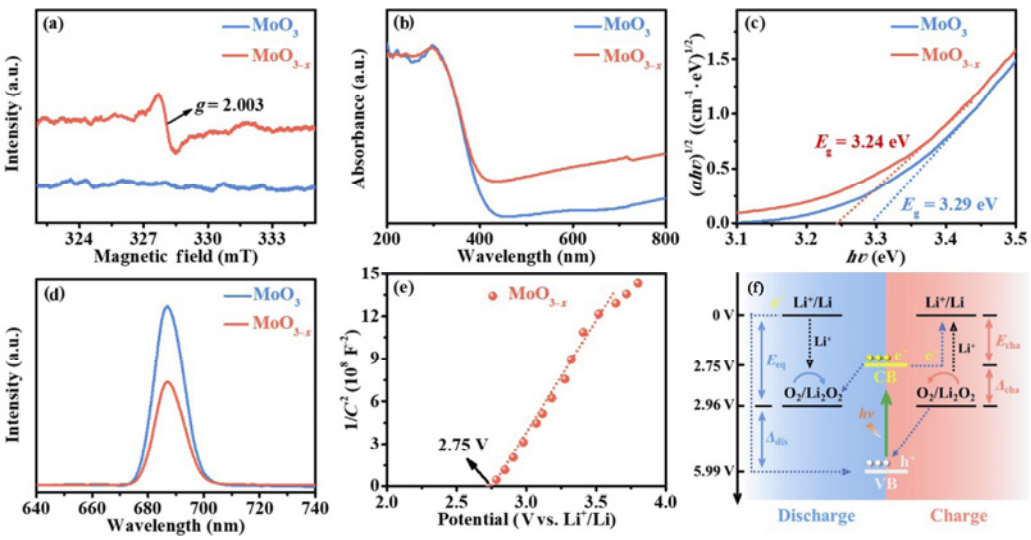


**Fig. 4** (a) ESR spectra, (b) UV–Vis spectra, (c) corresponding Kubelka–Munk-transformed spectra, and (d) PL spectra of $MoO_3$ and $MoO_{3-x}$ nanorods. (e) Mott–Schottky plot of $MoO_{3-x}$ nanorods. (f) Schematic energy diagram of Li–$O_2$ cell using $MoO_{3-x}$ nanorods as catalyst under illumination.

the holes in the VB can facilitate the decomposition of $Li_2O_2$, and the photoelectrons can reduce $Li^+$ at the anode by the external circuit. Thus, the $MoO_{3-x}$ nanorods are considered as promising photocatalysts for the photo-assisted Li–$O_2$ batteries.

To identify the effect of the oxygen vacancies on an electrochemical process of the photo-assisted Li–$O_2$ batteries, the CV curves of the cells using $MoO_3$ and $MoO_{3-x}$ nanorods as the catalysts with/without illumination were recorded in an $O_2$ atmosphere. As shown in Fig. 5(a), the cell with the $MoO_{3-x}$ nanorods under light shows a higher onset potential and larger anodic current in the ORR process as well as a lower onset potential and larger cathodic current in the OER process than those of the cell with the $MoO_{3-x}$ nanorods in dark and the cell with the $MoO_3$ nanorods under light, indicating the high ORR and OER activity of the $MoO_{3-x}$ nanorods under illumination [46,47]. Figure 5(b) shows the first galvanostatic discharge profiles of the Li–$O_2$ cells based on the $MoO_3$ and $MoO_{3-x}$ catalysts with/without illumination at 200 mA·g$^{-1}$ with a cutoff potential of 2.2 V. Discharge capacity of the cell with $MoO_{3-x}$ under light (4035 mAh·g$^{-1}$) is higher than those of the cell with $MoO_{3-x}$ in dark (2390 mAh·g$^{-1}$) and the cell with $MoO_3$ under light (3342 mAh·g$^{-1}$). Figure 5(c) depicts the first discharge and recharge curves of the cells with $MoO_3$ and $MoO_{3-x}$ nanorods at 100 mA·g$^{-1}$ with/without illumination. It can be seen that the discharge and charge potentials are 2.71 and 3.63 V for the cell with $MoO_{3-x}$ in dark, respectively, corresponding to round-trip efficiency of 74.66%. For the cell with $MoO_3$ under light, the discharge and charge potentials are 2.78 and 3.58 V, respectively, and the corresponding round-trip efficiency is 77.65%. For the cell with $MoO_{3-x}$ under light, an increased discharge potential of 2.86 V and a reduced charge potential of 3.08 V are obtained, which show ultrahigh round-trip efficiency of 92.86%. The rate performance of the Li–$O_2$ cells with $MoO_3$ and $MoO_{3-x}$ at various current density of 100, 200, and 500 mA·g$^{-1}$ is evaluated with/without illumination (Figs. 5(d)–5(f)). In Fig. 5(d), the overpotentials for the cell with $MoO_{3-x}$ under light are 0.22, 0.48, and 0.87 V at 100, 250, and 500 mA·g$^{-1}$, respectively, corresponding to the round-trip efficiency of 92.86%, 85.32%, and 75.69%, respectively. The slightly increased overpotential and reduced round-trip efficiency could be caused by the restricted photogenerated electrons contributing to the compensative current [15]. Note that the overpotentials for the cells with $MoO_{3-x}$ under light are still lower than those of the cells with $MoO_{3-x}$ in dark (Fig. 5(e)) and the cells with $MoO_3$ under light (Fig. 5(f)). Additionally, cyclability of the Li–$O_2$ cells with $MoO_3$ and $MoO_{3-x}$ catalysts were investigated at 250 mA·g$^{-1}$ under 500 mAh·g$^{-1}$ with/without illumination. Cycle life of the cell with $MoO_{3-x}$ reaches 100 cycles under light (Figs. 6(a) and 6(d)). In contrast, the cell with $MoO_{3-x}$ keeps 30 cycles in dark (Figs. 6(b) and 6(d)), and the cell with $MoO_3$

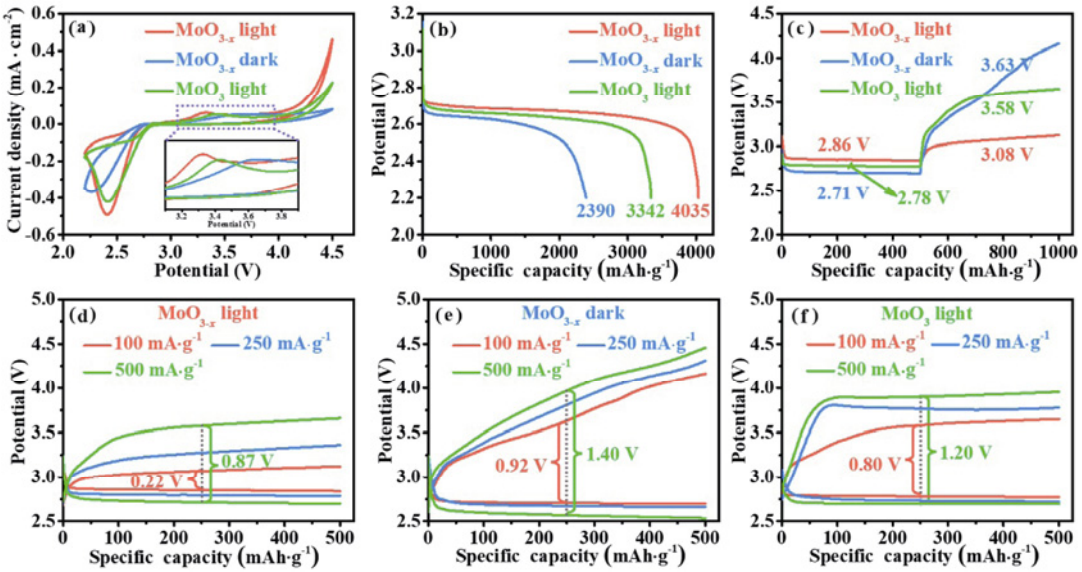


**Fig. 5** (a) CV curves of cells using $MoO_3$ and $MoO_{3-x}$ nanorods as catalysts with/without illumination; (b) discharge profiles of cells using $MoO_3$ and $MoO_{3-x}$ nanorods as catalysts with/without illumination; (c) first discharge and recharge curves of cells with $MoO_3$ and $MoO_{3-x}$ nanorods at 100 mA·g$^{-1}$ with/without illumination; (d–f) first discharge and charge curves of Li–$O_2$ cells with $MoO_3$ and $MoO_{3-x}$ at various current densitiy with/without illumination.

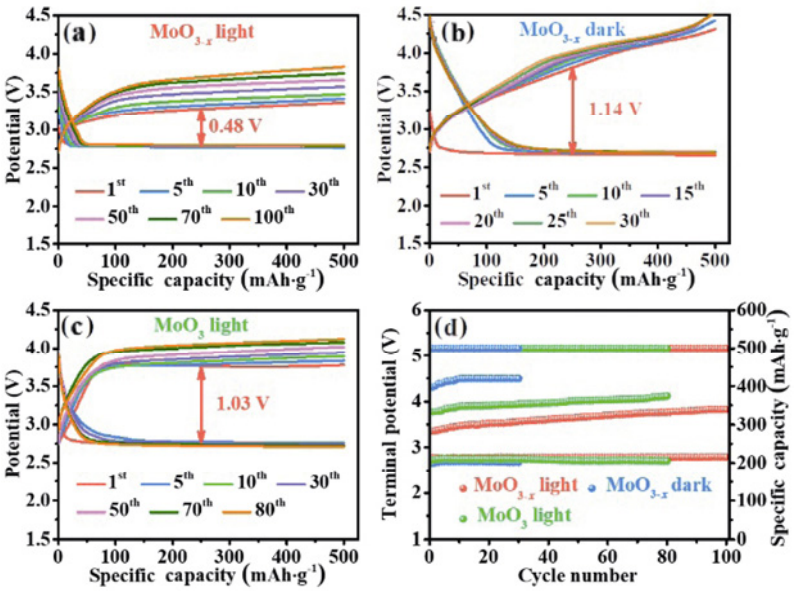


**Fig. 6** (a–c) Continuously discharge and charge curves of cells using $MoO_3$ and $MoO_{3-x}$ nanorods as catalysts with/without illumination; (d) corresponding cycle number associated with terminal discharge/charge voltage and delivered discharge.

shows 80 cycles under light (Figs. 6(c) and 6(d)). These results indicate that the $MoO_{3-x}$ nanorods as the catalyst are beneficial to facilitating the ORR and OER processes in the photo-assisted Li–$O_2$ batteries, demonstrating the advancement of introducing the oxygen vacancies into $MoO_3$.

Figure 7(a) shows LSV curves for the Li–$O_2$ cells using $MoO_3$ and $MoO_{3-x}$ nanorods as the catalysts at a scan rate of 0.5 mV·$s^{-1}$ within a potential range of 2.4–3.0 V with/without illumination. The cell with the $MoO_{3-x}$ nanorods under light exhibits an improved onset potential than those of the cell with the $MoO_{3-x}$ nanorods in dark and the cell with the $MoO_3$ nanorods under light, which suggests a positive effect of both oxygen vacancies and light assistance in the ORR process. Based on the LSV curves, Tafel slopes were obtained, as shown in Fig. 7(b). The cell with the $MoO_{3-x}$ nanorods under light shows a lower Tafel slope value of 117 mV·$dec^{-1}$ than those of the cell with the $MoO_{3-x}$ nanorods in dark of 194 mV·$dec^{-1}$ and the cell with the $MoO_3$ nanorods under light of 129 mV·$dec^{-1}$, proving a fast electron migration rate for the ORR process for the cell with the $MoO_{3-x}$ nanorods under light. Additionally, to assess the reaction kinetics of the $MoO_{3-x}$ nanorods under illumination during the OER process, the preloaded $Li_2O_2$ cells were prepared based on commercial $Li_2O_2$. The LSV curves for the preloaded $Li_2O_2$ cells using $MoO_3$ and $MoO_{3-x}$ nanorods as the catalysts at a scan rate of 0.5 mV·$s^{-1}$ within a potential range of 3.0–4.5 V with/without illumination are displayed in Fig. 7(c). It can be seen that the cell with the $MoO_{3-x}$ nanorods under light shows a lower onset potential and larger cathodic current than those of the cell with the $MoO_{3-x}$ nanorods in dark and the cell with the $MoO_3$ nanorods under light, indicating a positive effect of both oxygen vacancies and light assistance on the OER process. Equally, the Tafel slope of the cell with the $MoO_{3-x}$ nanorods under light was calculated to be 472 mV·$dec^{-1}$, which is lower than those of the cell with the $MoO_{3-x}$ nanorods in dark of 1469 mV·$dec^{-1}$ and the cell with the $MoO_3$ nanorods under light of 686 mV·$dec^{-1}$, further demonstrating a rapid electron migration rate of the OER process for the cell with the $MoO_{3-x}$ nanorods under light (Fig. 7(d)). Therefore, the cell with the $MoO_3$ nanorods under light exhibit superior reaction kinetics during the ORR and OER processes, which could be ascribed to the effect of both oxygen vacancies and light assistance.

The reversibility of the cell with the $MoO_{3-x}$ nanorods under illumination was investigated by the DEMS to characterize the gas consumption and formation during the galvanostatic cycle process. In Fig. 8(a), during the discharge process, the molar ratio of $e^-/O_2$ is calculated, which is 2.04, close to the theoretical value for the $O_2$ reduction to $Li_2O_2$. During the recharge process, the $CO_2$ release cannot be detected (Fig. 8(a)). Equally, the $O_2$ recovery efficiency is obtained to be 95.3% by calculating the area ratio of $O_2$ evolution and consumption curves (Figs. 8(a) and 8(b)). These results indicate that the cell with the $MoO_{3-x}$ nanorods shows good reversibility

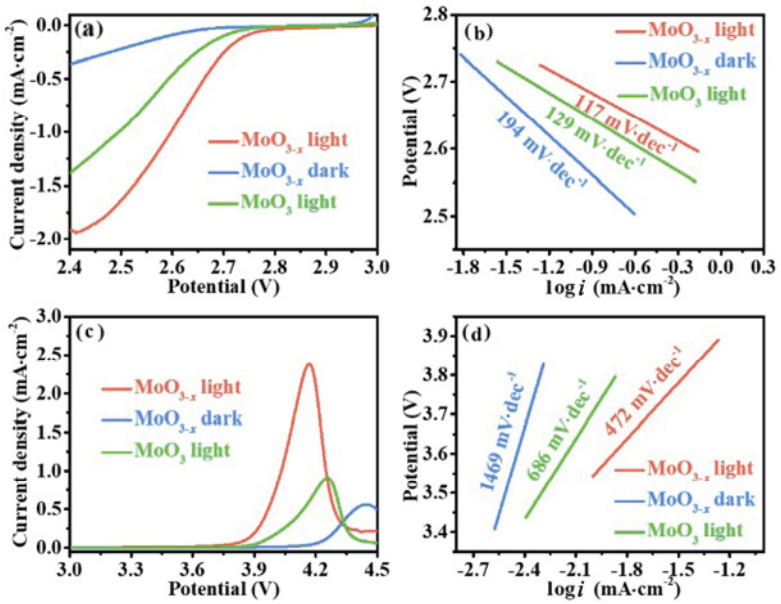


**Fig. 7** (a, c) LSV curves of the ORR and OER processes for cells using $MoO_3$ and $MoO_{3-x}$ nanorods as catalysts with/without illumination; (b, d) corresponding Tafel curves, where $i$ refers to the current density in (a, c).

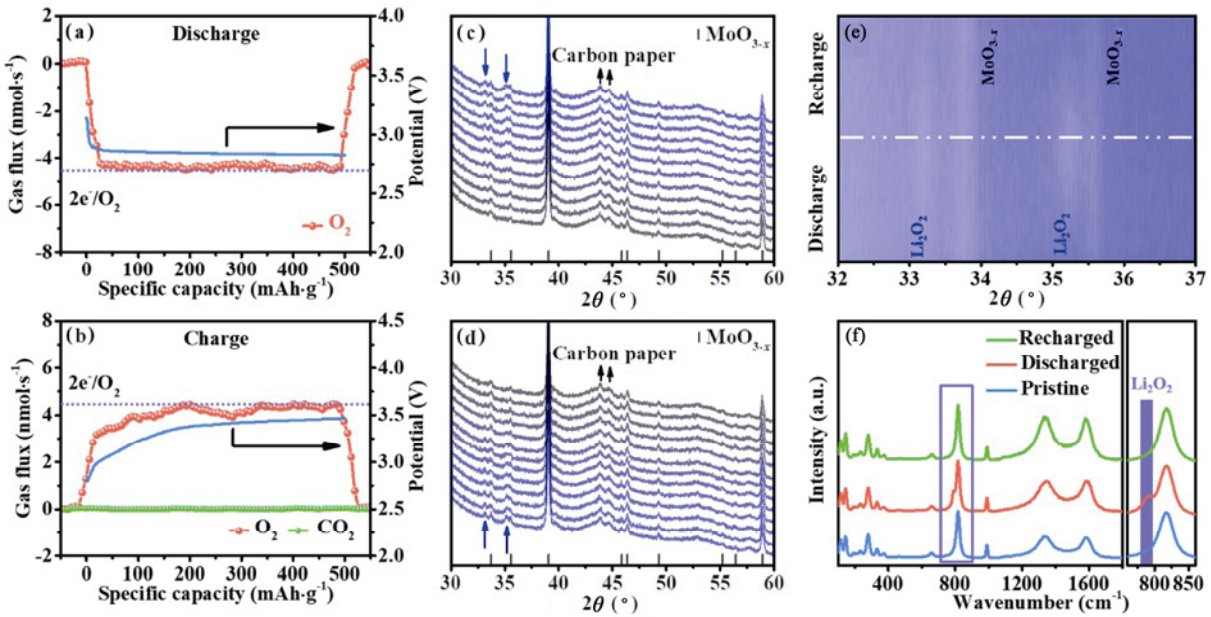


**Fig. 8** DEMS results of photo-assisted Li–$O_2$ batteries with $MoO_{3-x}$ nanorods for (a) discharge and (b) recharge processes; *in-situ* XRD patterns of cathode at (c) discharge and (d) recharge processes in photo-assisted Li–$O_2$ cell with $MoO_{3-x}$ nanorods and (e) corresponding contour mapping; (f) Raman spectra of cathodes at different electrochemical states.

under illumination. To identify the discharge products, the *in-situ* XRD is employed to track the cathode for the Li–$O_2$ cell with $MoO_{3-x}$ under illumination. In Fig. 8(c), during the discharge process, the diffraction peaks at 32.9° and 35.0° appear, and their intensity gradually increase, which are matched well with those of the $Li_2O_2$ standard pattern (PDF No. 09-0355), implying that the discharge product is $Li_2O_2$ [48]. In Fig. 8(d), the intensity of the $Li_2O_2$ diffraction peaks gradually reduce until the peaks disappear during the subsequent recharge process. Figure 8(e) shows the *in-situ* XRD contour mapping during cycling. Note that the typical diffraction peaks of $Li_2O_2$ appear during the discharge process and disappear after the recharge process, demonstrating that the generation and decomposition of $Li_2O_2$ are reversible during the discharge and charge processes. Additionally, we employed the Raman spectra to characterize the cathodes under different electrochemical

states, as shown in Fig. 8(f). After discharge, a peak at 788 $cm^{-1}$ is observed, further indicating that the discharge products are $Li_2O_2$ [49]. After recharge, the $Li_2O_2$ peak disappears, suggesting the complete decomposition of the formed $Li_2O_2$, which is consistent with the *in-situ* XRD results.

Morphology changes of $Li_2O_2$ are studied by the SEM to characterize the cathode at 100 $mA \cdot g^{-1}$ under different electrochemical states. Compared with that of the pristine cathode (Fig. S2(a) in the ESM), the SEM image of the discharged cathode shows that $Li_2O_2$ is film-like (Fig. 9(a)). As seen in Fig. 9(b), the film-like $Li_2O_2$ was completely removed after recharge. The film-like $Li_2O_2$ accumulates continuously after deep discharge, and their morphologies remain unchanged (Fig. S2(b) in the ESM). Note that the reversible formation and decomposition of $Li_2O_2$ could be maintained for up to 50 cycles, as shown in Figs. 9(c) and 9(d). Additionally, the morphologies of $Li_2O_2$ studied at high current density of 250 and 500 $mA \cdot g^{-1}$ were also studied, as shown in Fig. S3 in the ESM. It can be seen that the granular-like discharge products form on the film-like $Li_2O_2$ with the increase in the current density (Figs. S3(a) and S3(b) in the ESM). The granular-like discharge products completely disappear after recharge (Figs. S3(c) and S3(d) in the ESM). These results further evidence that the Li–$O_2$ cells with $MoO_{3-x}$ show superior reversibility under illumination.

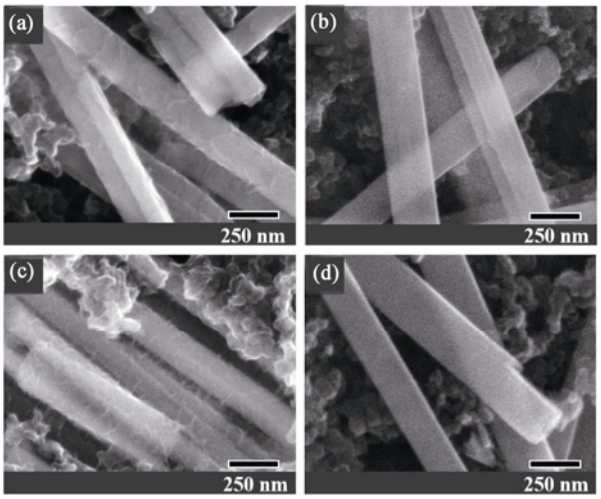


**Fig. 9** SEM images of cathode under different electrochemical states of (a) 1st discharged, (b) 1st recharged, (c) 50th discharged, and (d) 50th recharged for photo-assisted Li–$O_2$ cell with $MoO_{3-x}$ nanorods.

To study the catalytic and photovoltaic advantages of the $MoO_{3-x}$ nanorods, the EIS of the Li–$O_2$ cells were collected after different cycles without and with illumination, as shown in Figs. 10(a) and 10(b), respectively. The Nyquist plots present a semicircle and a diffusive part, which are the classical shape. The insets in Figs. 10(a) and 10(b) show the corresponding equivalent circuit, where $R_0$ represents the ohmic resistance, $R_{ct}$ corresponds to the charge transfer resistance, and CPE is the abbreviation of constant phase element [50]. The values

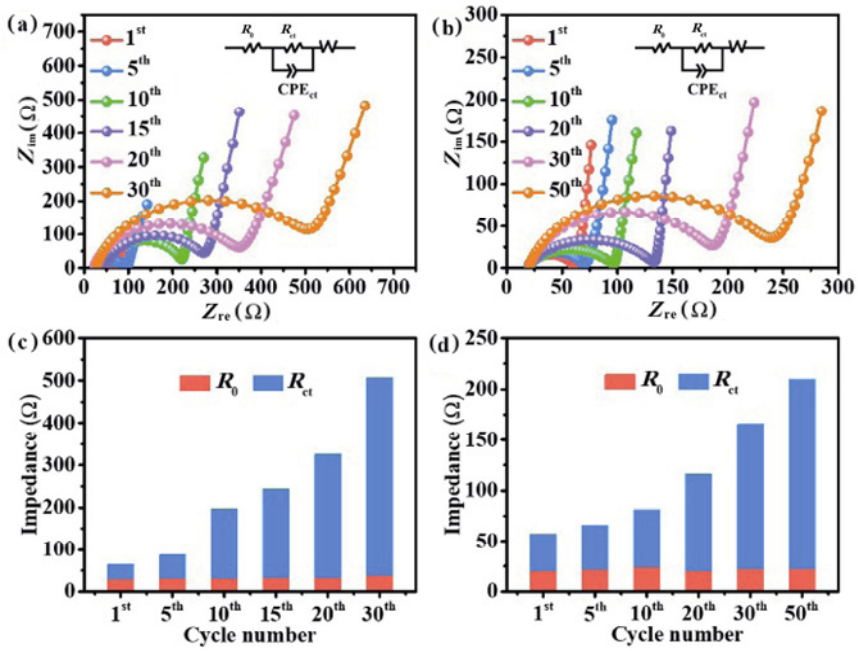


**Fig. 10** Nyquist plots of Li–$O_2$ cell with $MoO_{3-x}$ nanorods after different cycles (a) without and (b) with illumination where $Z_{im}$ is the imaginary part of the impedance, and $Z_{re}$ is the real part of the impedance; (c, d) corresponding fitting values of $R_0$ and $R_{ct}$.

of $R_0$, $R_{ct}$, and total resistance ($R_{total} = R_0 + R_{ct}$) are fitted by the equivalent circuit, as recorded in Table S1 in the ESM and Figs. 10(c) and 10(d). The values of $R_{ct}$ and $R_{total}$ increase clearly from the 1st to 30th cycle for the cell cycled with $MoO_{3-x}$ in dark. In contrast, the values of $R_{ct}$ and $R_{total}$ increase slowly until 50 cycles for the cell with $MoO_{3-x}$ cycled in light. These results further indicate that the $MoO_{3-x}$ nanorods with high photoelectro-catalytic activity can improve the electrochemical microenvironment of the photo-assisted Li–$O_2$ cells and thus accelerate the reaction kinetics.

## 4 Conclusions

In summary, $MoO_{3-x}$ nanorods were successfully synthesized by combining the solvothermal method and hydrogen-thermal reduction method. In photo-assisted Li–$O_2$ batteries, the $MoO_{3-x}$ nanorods as photocatalysts not only help to lower the overpotential, but also boost the discharge capacity. The *in-situ* XRD, *ex-situ* measurements, and electroanalytic techniques indicated that the advanced performance of the photo-assisted Li–$O_2$ batteries could be ascribed to the super photocatalytic ability of the $MoO_{3-x}$ nanorods in affording the reversible formation and decomposition of $Li_2O_2$. The photoexcited electrons and holes on the $MoO_{3-x}$ nanorods are separated effectively under light illumination, which can boost the ORR/OER process and improve the electrochemical microenvironment. As a result, the photo-assisted Li–$O_2$ batteries with the $MoO_{3-x}$ nanorods show an ultralow overpotential of 0.22 V and ultrahigh round-trip efficiency of 92.86%. We hope that the work can make a contribution to the exploitation of the efficient catalysts for photo-assisted Li–$O_2$ batteries.

### Acknowledgements

This work was supported by the Jilin Province Science and Technology Department Program (Nos. YDZJ202101ZYTS047, YDZJ202201ZYTS304, 20220201130GX, and 20200201187JC), the National Natural Science Foundation of China (Nos. 52171210 and 21978110), and the Science and Technology Project of Jilin Provincial Education Department (Nos. JJKH20210444KJ and JJKH20220428KJ).

### Declaration of competing interest

The authors have no competing interests to declare that are relevant to the content of this article.

### Electronic Supplementary Material

Supplementary material is available in the online version of this article at https://doi.org/10.26599/JAC.2023.9220717.

### References

[1] Huang G, Wang J, Zhang XB. Electrode protection in high-efficiency Li–$O_2$ batteries. *ACS Cent Sci* 2020, **6**: 2136–2148.

[2] Wu C, Yang QR, Zheng Z, *et al*. Boosting Na–$O_2$ battery performance by regulating the morphology of $NaO_2$. *Energy Storage Mater* 2023, **54**: 1–9.

[3] Kwak WJ, Rosy, Sharon D, *et al*. Lithium–oxygen batteries and related systems: Potential, status, and future. *Chem Rev* 2020, **120**: 6626–6683.

[4] Hu XL, Luo G, Zhao QN, *et al*. Ru single atoms on N-doped carbon by spatial confinement and ionic substitution strategies for high-performance Li–$O_2$ batteries. *J Am Chem Soc* 2020, **142**: 16776–16786.

[5] Liu YQ, Hou YY, Liu LL, *et al*. Nanostructured carbon-based cathode materials for non-aqueous Li–$O_2$ batteries. *Mater Lab* 2022, **1**: 220015.

[6] Gao R, Zhou D, Ning D, *et al*. Probing the self-boosting catalysis of $LiCoO_2$ in Li–$O_2$ battery with multiple *in situ*/operando techniques. *Adv Funct Mater* 2020, **30**: 2002223.

[7] Zhao Q, Katyal N, Seymour ID, *et al*. Vanadium(III) acetylacetonate as an efficient soluble catalyst for lithium–oxygen batteries. *Angew Chem Int Ed* 2019, **58**: 12553–12557.

[8] He B, Li GY, Li JJ, *et al*. $MoSe_2$@CNT core–shell nanostructures as grain promoters featuring a direct $Li_2O_2$ formation/decomposition catalytic capability in lithium–oxygen batteries. *Adv Energy Mater* 2021, **11**: 2003263.

[9] Liu XM, Huang QS, Wang J, *et al*. *In-situ* deposition of Pd/$Pd_4S$ heterostructure on hollow carbon spheres as efficient electrocatalysts for rechargeable Li–$O_2$ batteries. *Chinese Chem Lett* 2021, **32**: 2086–2090.

[10] Jeong YS, Park JB, Jung HG, *et al*. Study on the catalytic activity of noble metal nanoparticles on reduced graphene oxide for oxygen evolution reactions in lithium–air batteries. *Nano Lett* 2015, **15**: 4261–4268.

[11] Sun GR, Li F, Wu T, *et al*. $O_2$ adsorption associated with sulfur vacancies on $MoS_2$ microspheres. *Inorg Chem* 2019, **58**: 2169–2176.

[12] Zhang GL, Li GY, Wang J, *et al*. 2D SnSe cathode catalyst featuring an efficient facet-dependent selective $Li_2O_2$ growth/decomposition for Li–oxygen batteries. *Adv Energy Mater* 2022, **12**: 2103910.

[13] Lv QL, Zhu Z, Zhao S, *et al*. Semiconducting metal-organic polymer nanosheets for a photoinvolved Li–$O_2$

battery under visible light. *J Am Chem Soc* 2021, **143**: 1941–1947.
[14] Jiao HL, Sun GR, Wang Y, *et al*. Defective $TiO_2$ hollow nanospheres as photo-electrocatalysts for photo-assisted Li–$O_2$ batteries. *Chinese Chem Lett* 2022, **33**: 4008–4012.
[15] Li ML, Wang XX, Li F, *et al*. A bifunctional photo-assisted Li–$O_2$ battery based on a hierarchical heterostructured cathode. *Adv Mater* 2020, **32**: 1907098.
[16] Li DW, Lang XY, Guo Y, *et al*. A photo-assisted electrocatalyst coupled with superoxide suppression for high performance Li–$O_2$ batteries. *Nano Energy* 2021, **85**: 105966.
[17] Zulfiqar S, Liu S, Rahman N, *et al*. Construction of S-scheme $MnO_2$@CdS heterojunction with core–shell structure as $H_2$-production photocatalyst. *Rare Met* 2021, **40**: 2381–2391.
[18] Cheng Q, Zhang GK. Enhanced photocatalytic performance of tungsten-based photocatalysts for degradation of volatile organic compounds: A review. *Tungsten* 2020, **2**: 240–250.
[19] Jia CY, Zhang F, She LN, *et al*. Ultra-large sized siloxene nanosheets as bifunctional photocatalyst for a Li–$O_2$ battery with superior round-trip efficiency and extra-long durability. *Angew Chem Int Ed* 2021, **60**: 11257–11261.
[20] Xue HR, Wang T, Feng YY, *et al*. Efficient separation of photoexcited carriers in a g-$C_3N_4$-decorated $WO_3$ nanowire array heterojunction as the cathode of a rechargeable Li–$O_2$ battery. *Nanoscale* 2020, **12**: 18742–18749.
[21] Hu FY, Zhang F, Wang XH, *et al*. Ultrabroad band microwave absorption from hierarchical $MoO_3$/$TiO_2$/$Mo_2TiC_2T_x$ hybrids via annealing treatment. *J Adv Ceram* 2022, **11**: 1466–1478.
[22] Zhu YH, Yao Y, Luo Z, *et al*. Nanostructured $MoO_3$ for efficient energy and environmental catalysis. *Molecules* 2019, **25**: 18.
[23] Hu C, Xu MJ, Zhang J, *et al*. Recyclable $MoO_3$ nanobelts for photocatalytic degradation of rhodamine B by near infrared irradiation. *Int J Chem Kinet* 2019, **51**: 3–13.
[24] Hussain MK, Khalid NR. Surfactant-assisted synthesis of $MoO_3$ nanorods and its application in photocatalytic degradation of different dyes in aqueous environment. *J Mol Liq* 2022, **346**: 117871.
[25] Sajadi M, Ranjbar M, Rasuli R. Two-step synthesis of Ag-decorated $MoO_3$ nanotubes, and the effect of hydrogen doping. *Appl Surf Sci* 2020, **527**: 146675.
[26] Zhou Z, Wang YL, Peng F, *et al*. Intercalation-activated layered $MoO_3$ nanobelts as biodegradable nanozymes for tumor-specific photo-enhanced catalytic therapy. *Angew Chem Int Ed* 2022, **61**: e202115939.
[27] Liu QW, Wu YW, Zhang JW, *et al*. Plasmonic $MoO_{3-x}$ nanosheets with tunable oxygen vacancies as efficient visible light responsive photocatalyst. *Appl Surf Sci* 2019, **490**: 395–402.
[28] Chen YY, Zhang Y, Zhang X, *et al*. Self-templated fabrication of $MoNi_4$/$MoO_{3-x}$ nanorod arrays with dual active components for highly efficient hydrogen evolution. *Adv Mater* 2017, **29**: 1703311.
[29] Zhang SP, Wang G, Jin J, *et al*. Self-catalyzed decomposition of discharge products on the oxygen vacancy sites of $MoO_3$ nanosheets for low-overpotential Li–$O_2$ batteries. *Nano Energy* 2017, **36**: 186–196.
[30] Hanson ED, Lajaunie L, Hao SQ, *et al*. Systematic study of oxygen vacancy tunable transport properties of few-layer $MoO_{3-x}$ enabled by vapor-based synthesis. *Adv Funct Mater* 2017, **27**: 1605380.
[31] Ji FX, Ren XP, Zheng XY, *et al*. 2D-$MoO_3$ nanosheets for superior gas sensors. *Nanoscale* 2016, **8**: 8696–8703.
[32] Alsaif MMYA, Latham K, Field MR, *et al*. Tunable plasmon resonances in two-dimensional molybdenum oxide nanoflakes. *Adv Mater* 2014, **26**: 3931–3937.
[33] Ou JZ, Campbell JL, Yao D, *et al*. *In situ* Raman spectroscopy of $H_2$ gas interaction with layered $MoO_3$. *J Phys Chem C* 2011, **115**: 10757–10763.
[34] Zhang YY, Chen P, Wang QY, *et al*. High-capacity and kinetically accelerated lithium storage in $MoO_3$ enabled by oxygen vacancies and heterostructure. *Adv Energy Mater* 2021, **11**: 2101712.
[35] Chu K, Luo YJ, Shen P, *et al*. Unveiling the synergy of O-vacancy and heterostructure over $MoO_{3-x}$/MXene for $N_2$ electroreduction to $NH_3$. *Adv Energy Mater* 2022, **12**: 2103022.
[36] Wang FH, Dong BB, Wang JW, *et al*. Self-supported porous heterostructure WC/$WO_{3-x}$ ceramic electrode for hydrogen evolution reaction in acidic and alkaline media. *J Adv Ceram* 2022, **11**: 1208–1221.
[37] Luo Z, Miao R, Huan TD, *et al*. Mesoporous $MoO_{3-x}$ material as an efficient electrocatalyst for hydrogen evolution reactions. *Adv Energy Mater* 2016, **6**: 1600528.
[38] Liu XF, Luo YN, Ling CC, *et al*. Rare earth La single atoms supported $MoO_{3-x}$ for efficient photocatalytic nitrogen fixation. *Appl Catal B-Environ* 2022, **301**: 120766.
[39] Guan X, Ren YB, Chen SF, *et al*. Charge separation and strong adsorption-enhanced $MoO_3$ visible light photocatalytic performance. *J Mater Sci* 2020, **55**: 5808–5822.
[40] Li YB, Jin ZL, Wang HY, *et al*. Effect of electron-hole separation in $MoO_3$@$Ni_2P$ hybrid nanocomposite as highly efficient metal-free photocatalyst for $H_2$ production. *J Colloid Interf Sci* 2019, **537**: 629–639.
[41] Mohamed MM, Salama TM, Morsy M, *et al*. Facile strategy of synthesizing α-$MoO_{3-x}$ nanorods boosted as traced by 1% graphene oxide: Efficient visible light photocatalysis and gas sensing applications. *Sensor Actuat B-Chem* 2019, **299**: 126960.
[42] Wei L, Su YH, Ma Y, *et al*. Photoluminescent $WSe_2$ nanofibers as freestanding cathode for solar-assisted Li–$O_2$ battery with ultrahigh capacity and transparent casing. *Chem Eng J* 2022, **448**: 137591.
[43] Shang YY, Chen X, Liu WW, *et al*. Photocorrosion inhibition and high-efficiency photoactivity of porous g-$C_3N_4$/$Ag_2CrO_4$ composites by simple microemulsion-assisted co-precipitation method. *Appl Catal B-Environ* 2017, **204**: 78–88.
[44] Zheng F, Dong FQ, Lv ZZ, *et al*. A novel g-$C_3N_4$/ tourmaline

composites equipped with plasmonic $MoO_{3-x}$ to boost photocatalytic activity. *Colloid Interf Sci* 2021, **43**: 100434.
[45] Huang LY, Xu H, Zhang RX, *et al*. Synthesis and characterization of g-$C_3N_4$/$MoO_3$ photocatalyst with improved visible-light photoactivity. *Appl Surf Sci* 2013, **283**: 25–32.
[46] Zhang GL, Liu CY, Guo L, *et al*. Electronic "bridge" construction via Ag intercalation to diminish catalytic anisotropy for 2D tin diselenide cathode catalyst in lithium–oxygen batteries. *Adv Energy Mater* 2022, **12**: 2200791.
[47] Guo L, Tan LW, Xu AL, *et al*. Highly efficient two-dimensional $Ag_2Te$ cathode catalyst featuring a layer structure derived catalytic anisotropy in lithium–oxygen batteries. *Energy Storage Mater* 2022, **50**: 96–104.
[48] Sun GR, Gao R, Jiao HL, *et al*. Self-formation CoO nanodots catalyst in $Co(TFSI)_2$-modified electrolyte for high efficient Li–$O_2$ batteries. *Adv Mater* 2022, **34**: 2201838.
[49] Zhao Q, Wu CX, Cong LN, *et al*. Yolk–shell $Co_2CrO_4$ nanospheres as highly active catalysts for Li–$O_2$ batteries: Understanding the electrocatalytic mechanism. *J Mater Chem A* 2017, **5**: 544–553.
[50] Liu J, Wu T, Zhang SQ, *et al*. $InBr_3$ as a self-defensed redox mediator for Li–$O_2$ batteries: *in situ* construction of a stable indium-rich composite protective layer on the Li anode. *J Power Sources* 2019, **439**: 227095.